Direct reservoir parameter estimation using joint inversion of marine seismic AVA and CSEM data

G. Michael Hoversten[1], Florence Cassassuce[1], Erika Gasperikova[1], Gregory A. Newman[1], Jinsong Chen[1], Yoram Rubin[2], Zhangshuan Hou[2], and Don Vasco[1]

ABSTRACT

Accurately estimating reservoir parameters from geophysical data is vitally important in hydrocarbon exploration and production. We have developed a new joint-inversion algorithm to estimate reservoir parameters directly, using both seismic amplitude variation with angle of incidence (AVA) data and marine controlled-source electromagnetic (CSEM) data. Reservoir parameters are linked to geophysical parameters through a rock-properties model. Errors in the parameters of the rock-properties model introduce errors of comparable size in the reservoir-parameter estimates produced by joint inversion. Tests of joint inversion on synthetic 1D models demonstrate improved fluid saturation and porosity estimates for joint AVA-CSEM data inversion (compared with estimates from AVA or CSEM inversion alone). A comparison of inversions of AVA data, CSEM data, and joint AVA-CSEM data over the North Sea Troll field, at a location for which we have well control, shows that the joint inversion produces estimates of gas saturation, oil saturation, and porosity that are closest (as measured by the rms difference, the L_1 norm of the difference, and net values over the interval) to the logged values. However, CSEM-only inversion provides the closest estimates of water saturation.

INTRODUCTION

Estimation of reservoir parameters from geophysical data is the goal of most geophysical surveys performed in the context of hydrocarbon exploration and production. In recent years, the focus has been on using time-lapse seismic data for predicting changes in pressure and fluid saturation (Tura and Lumley, 1999; Landro,

2001; Lumley et al., 2003). Changes in pore pressure (P_p) and water saturation (S_w) can be predicted when we have only oil saturation (S_o) and S_w with which to work, because we are deriving just two independent variables, P_p and either S_w or S_o ($S_o + S_w = 1$), from two data (acoustic impedance and shear impedance). The presence of gas complicates the problem by introducing a third independent variable, gas saturation (S_g).

Another interesting case arises in exploration for economic gas deposits, where determining the level of S_g is critical. Although we can estimate S_w and S_o using the variation of reflection amplitudes as a function of source-receiver offset (AVO) or of angle (AVA), its use for estimating S_g is more problematic. Castagna (1993) summarized the use of AVO for seismic gas exploration: "According to Gassmann's equations, a gas sand with 1% gas saturation can have the same V_p/V_s as a commercial accumulation of gas. Thus, unless density can be accurately extracted utilizing far-offset information, AVO cannot distinguish commercial and noncommercial gas accumulations."

Subsequent research on inversion of AVA data to predict seismic parameters (Debski and Tarantola, 1995; Drufuca and Mazzotti, 1995; Plessix and Bork, 2000; Buland and More, 2003) concluded that density is the least well-determined parameter in any form of AVA inversion and cannot be estimated reliably for practical purposes. Thus, we cannot use current seismic technology to distinguish economic from noneconomic gas accumulations accurately, and that failure results in significant exploration losses.

A simple rock-property-modeling exercise illustrates the relative sensitivity of AVO data to gas saturation and porosity of sand encased in shale. We used parameters for sand and shale obtained from a log from the Troll field, North Sea, to be discussed below. To calculate the V_p, V_s, and density (ρ) as a function of S_g and porosity (ϕ), in a brine-gas system at reservoir conditions, we used the rock-properties model for unconsolidated sand that Dvorkin and Nur (1996) described. We calculated the AVO intercept (A) and slope (B) (Aki and Richards, 1980) from V_p, V_s, and ρ.

To see the sensitivity of A and B to changes in S_g and ϕ, the changes (Δ) in A and B were calculated for values of S_g and ϕ that are an increment above and below reference values of $S_g = 0.5$ and $\phi = 0.2$. Figure 1 presents maps of the changes in S_g and ϕ. The contour intervals are 0.1 in S_g (over the range 0.0–1.0) and 0.02 in ϕ (over the range 0.1–0.3), so each contour interval represents a 20% change in S_g and a 10% change in ϕ. In Figure 1, the origin corresponds to the reference case ($S_g = 0.5$, $\phi = 0.2$). The calculations show that increasing S_g by 20% (from 0.5 to 0.6) would produce a 3.1% decrease in A and a 0.22% increase in B (Figure 1a). By contrast, increasing ϕ by 10% (from 0.20 to 0.22) would produce a 158% decrease in A and an 8% decrease in B (Figure 1b).

Our calculations can be recast in terms of changes in V_p and V_s or in terms of changes in acoustic impedance and shear impedance, with the same relative importance of ϕ versus S_g. We conclude that differences in AVO parameters A and B, or V_p and V_s, or acoustic and shear impedance produced by differences in S_g (excluding S_g values in the range of 0.0 to 0.1), are too small to be estimated accurately, given realistic noise levels of seismic data. On the other hand, differences in AVO parameters A and B, or V_p and V_s, or acoustic and shear impedance produced by differences in ϕ, are one to two orders of magnitude larger than those produced by differences in S_g and should be estimable from high-quality seismic data.

In contrast to the insensitivity to gas saturation that is exhibited by seismic attributes such as V_p-V_s, AVO slope and intercept, or acoustic-shear impedance, the electrical resistivity of reservoir rocks is highly sensitive to S_g, through the link to water saturation. That sensitivity can be shown using Archie's law (Archie, 1942), which has been demonstrated to accurately describe the electrical resistivity of sedimentary rocks. Figure 2 shows the bulk resistivity (R_{bulk}) as a function of $S_g = (1 - S_w)$ for a sand having 25% porosity and brine salinity of 0.07 ppm at 60°C ($R_w = 0.05$ ohm-m). Porosity and S_w exponents of -2 are assumed for this calculation. The relationship between R_{bulk} and S_g has the advantage that the steepest slope in R_{bulk} occurs in the S_g range from 0.5 to 1.0, where the division between economic and noneconomic S_g usually occurs.

Recently, means of estimating R_{bulk} have become available through the use of controlled-source electromagnetic sounding systems. Over the last decade, developments in the petroleum application of marine electromagnetic systems were driven primarily by the need for structural information in areas where high-velocity materials such as salt or basalt covered prospective sediments. Both CSEM and passive-source magnetotelluric (MT) systems were considered for petroleum-related exploration (Hoversten and Unsworth, 1994). Workers noted from the beginning that CSEM systems have superior resolving capabilities when compared with MT.

However, the logistics of deployment and ease of data interpretation favored MT and resulted in a preponderance of work on marine MT systems (Hoversten et al., 1998; Constable et al., 1998; Hoversten et al., 2000). Development of CSEM systems actually predates marine MT systems; CSEM was used over the last two decades for investigations of deep-ocean crust (Constable, 1990; Constable and Cox, 1996; MacGregor et al., 2001). Seismic and CSEM data have been recorded coincidently in exploration of mid-ocean ridges (Webb and Forsyth, 1998; Evans et al., 1999) but have not been inverted simultaneously for a common model. Recently, attention has focused on the use of CSEM systems to directly detect and map hydrocarbons (Ellingsrud et al., 2002).

A marine CSEM system consists of a ship-towed electric dipole source and many seafloor-deployed recording instruments capable of recording orthogonal electric fields. In the last few years, several contractors have begun offering marine CSEM data on a commercial basis. Marine CSEM data can enhance the prediction of reservoir parameters, compared with industry-standard AVA techniques alone, because CSEM is highly sensitivity to water saturation.

In this paper, we illustrate the benefits of joint AVA-CSEM inversion for estimating fluid saturations and porosity from synthetic and field data. Joint inversion of various forms of seismic and electrical or electromagnetic data was presented for cross-borehole configuration by Tseng and Lee (2001) and for land-based seismic traveltime tomography and electrical resistivity by Gallardo and Meju (2003). Both of those studies demonstrated, as we do, that improved model-parameter estimates are obtained from the joint inversion compared with estimates from inversion of either seismic or electrical/electromagnetic data sets in isolation.
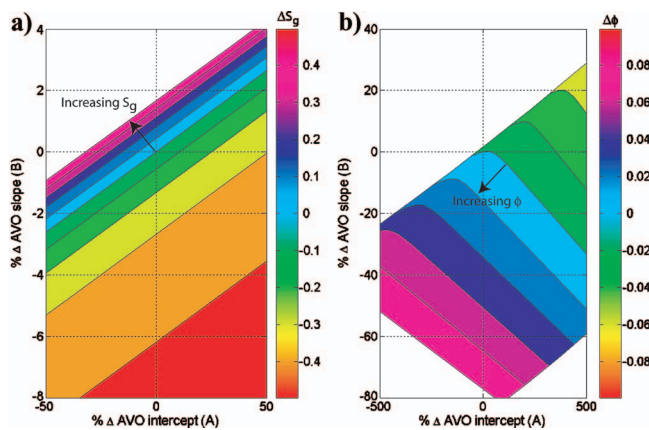

Figure 1. The reference point for calculations is porosity (ϕ) = 0.2, gas saturation (S_g) = 0.5. (a) Color contours of ΔS_g as a function of $\%\Delta$ AVO intercept (A) and $\%\Delta$ AVO slope (B). (b) Color contours of $\Delta\phi$ as a function of $\%\Delta A$ and $\%\Delta B$. Note that the axes for ΔS_g are a factor of 10 smaller than those for $\Delta\phi$.
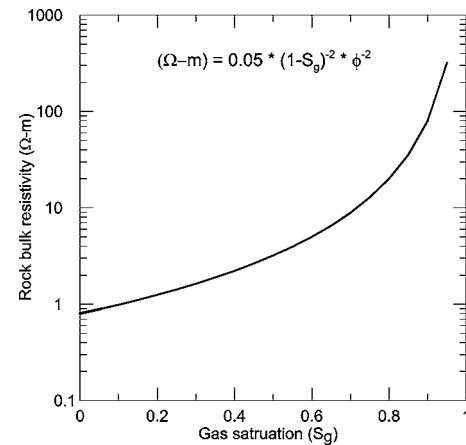

Figure 2. Rock bulk resistivity calculated from Archie's law. R_w = 0.05 for 0.07 ppm salinity, at 60°C, using porosity and S_w exponents of -2.

MODEL PARAMETERIZATION

The nature of seismic-source-generated energy propagation in the earth differs substantially from that generated by a CSEM source. Of particular importance to joint inversion of seismic AVA and marine CSEM data is the high attenuation of electromagnetic energy compared with the attenuation of seismic energy. After appropriate seismic processing (including amplitude recovery), we will assume that we have accounted for the seismic attenuation in the earth above the target interval (the overburden). In addition, we assume that the transmission loss through the model is small enough that the seismic response can be modeled as a convolution of a wavelet and a set of reflection coefficients over only the depth interval of interest.

However, for modeling the CSEM data, energy loss in the overburden is significant and affects the target zone's response, which cannot be estimated independently of the overburden (in any processing steps). This means that CSEM calculations require a model with electrical conductivity described from the sea surface down (an infinite air layer is also included), whereas seismic calculations only require that the reflection coefficients be calculated over the area of interest.

Because the CSEM and AVA calculations require different depth intervals in the model, we chose to parameterize the model as illustrated in Figure 3. Layers of variable thickness (layer thickness can be an inversion parameter) are common to all zones of the inversion domain. The layers of variable thickness are common to both the CSEM and AVA calculations.

The electrical conductivities of layers (σ) from the air-sea interface to the top of the reservoir interval are parameters. A zone above the reservoir interval is parameterized by V_p, V_s, and density (ρ). The reservoir interval is parameterized by porosity (ϕ) and fluid saturations (S_w, S_g, S_o). Pore pressure also is included in the inversion algorithm but is assumed to be constant for the examples shown here. Below the reservoir, layers are parameterized again by σ, V_p, V_s, and ρ.

Above the target zone, σ is required for the solution of the CSEM forward problem. The parameters V_p, V_s, and ρ of the overburden above the target are required for two reasons. First, the time interval for the seismic data used in the inversion is chosen from a time-to-depth conversion based on the available velocity model, which may be in error. If the depth to the top of the target (reservoir) zone does not tie exactly to the selected time window, the inversion can adjust V_p above the target zone as a correction.

Second, log information required to calculate the rock-properties model usually is taken only within the reservoir; therefore, we can only describe the target zone itself in terms of fluid saturations and ϕ. However, we need properties for the layer directly above the reservoir so we can calculate the reflection coefficient at the top of the reservoir. The V_p, V_s, and ρ below the target interval are not strictly required, but they provide continuity in the seismic-data fit at times below the reservoir.

INVERSION ALGORITHM

We chose to cast the inversion as a nonlinear least-squares problem, in which we minimize the Tikhonov functional (Tikhonov and Arsenin, 1977)

$$\theta = 1/2\{[F(\mathbf{m}) - \mathbf{d}^{obs}]\}^T \mathbf{D}^{-1}\{[F(\mathbf{m}) - \mathbf{d}^{obs}]\}$$
$$+ \lambda/2(\mathbf{m}^T\mathbf{W}^T\mathbf{W}\mathbf{m}), \tag{1}$$

where T denotes the transpose. The model-parameter vector $\mathbf{m}$ contains the V_p, V_s, density, conductivity, and thickness of the layers. The term $\mathbf{W}$ is a regularization matrix (we use the first spatial derivatives of the model parameters) that does not depend on $\mathbf{m}$, and $F(\mathbf{m})$ is the forward model that produces a calculated response to be matched to the observed data, $\mathbf{d}^{obs}$. The observed data $\mathbf{d}^{obs}$ contain the AVA traces for each angle and the CSEM data for each frequency and source-receiver offset. The data covariance matrix $\mathbf{D}$ has estimated data variances on the diagonal and zeros off the diagonal. Buland et al. (1996) applied Levenberg-Marquardt damped least squares to the AVO inversion of data from the Troll field, where their algorithm uses the identity matrix rather than ($\mathbf{m}^T\mathbf{W}^T\mathbf{W}\mathbf{m}$) in equation 1.

The above approach often is referred to as a local optimization (Tarantola, 1987), as opposed to a global optimization (Sen and Stoffa, 1995). Although a global approach is preferable for problems in which the computational costs of the forward problems are low, forward problems become impractical when the forward calculations become time- and/or memory-intensive. The amount of time and memory that is considered excessive increases each year, with the advance of computer technology. In general, however, any multidimensional geophysical forward problem involving wave propagation still is too much for most global inverse applications. The work we report here represents the first steps in a larger program to develop 3D joint seismic-CSEM inversion, and as such, the algorithms are to be applied to 3D forward problems in the future.

One-dimensional seismic AVA modeling uses the Zoeppritz equation (Aki and Richards, 1980) to calculate angle-dependent reflectivity, which is convolved with an angle-dependent wavelet to form the calculated seismic data. The CSEM calculations are an integral equation solution for the electric field (E) from an electric dipole source located within a layered medium (Ward and Hohmann, 1987). These forward models provide the derivatives of data with respect to the geophysical parameters (V_p, V_s, ρ, and σ) that form the Jacobian ($\mathbf{J}$) of normal geophysical inverse problems. The chain rule for derivatives is used to calculate the derivatives of the
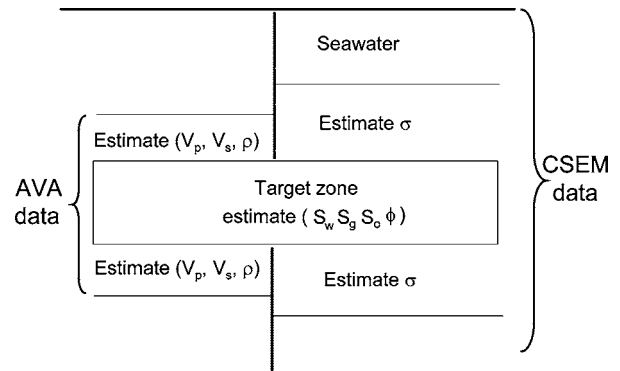

Figure 3. The inversion domain. The target zone is parameterized by S_g, S_w, and ϕ and is surrounded by V_p, V_s, and the density zone for the AVA data and surrounded by the conductivity zone for CSEM data.

object function to be minimized (θ) with respect to the reservoir parameters. The equation

$$\frac{\partial \theta}{\partial S_g} = \frac{\partial \theta}{\partial \sigma} \cdot \frac{\partial \sigma}{\partial S_g} + \frac{\partial \theta}{\partial V_p} \cdot \frac{\partial V_p}{\partial S_g} + \frac{\partial \theta}{\partial V_s} \cdot \frac{\partial V_s}{\partial S_g} + \frac{\partial \theta}{\partial \rho} \cdot \frac{\partial \rho}{\partial S_g} \tag{2}$$

shows the derivative of θ with respect to S_g in terms of all the required partial derivatives. The first half of each term on the right of equation 2 comes from the geophysics, and the second half comes from the rock-properties model.

The partial derivatives that relate changes in geophysical data to changes in model parameters are calculated by finite-differencing the forward solutions about the current model for fast 1D problems, and by the adjoint method for the CSEM portion of the problem using finite-difference methods for 3D problems (Newman and Hoversten, 2000). The model's parameters can be any reservoir parameter (i.e., water saturation, oil saturation, gas saturation, porosity, and pore pressure). In the examples we present in this paper, fluid saturations and porosity are considered to be inversion parameters. For the field data considered, the effects of pore pressure within realistic ranges for the Troll Reservoir are of second order compared with the effects of fluid saturations and porosity, and hence the pore-pressure effects are held constant in all inversions.

Linearizing equation 1 about a given model, $\mathbf{m}_i$, at the ith iteration, produces the quadratic form

$$(\mathbf{J}^T\mathbf{S}^T\mathbf{S}\mathbf{J} + \lambda\mathbf{W}^T\mathbf{W} + \alpha\mathbf{C}^T\mathbf{C})\mathbf{m}_{i+1}$$
$$= \mathbf{J}^T\mathbf{S}^T\mathbf{S}\mathbf{J}\mathbf{m}_i + \mathbf{J}^T\mathbf{S}^T\mathbf{S}\delta\mathbf{d}_i + \alpha\mathbf{C}^T\mathbf{h}, \tag{3}$$

where $\mathbf{m}_{i+1}$ is solved for using a quadratic programming algorithm (Fletcher and Jackson, 1974) that allows for upper and lower bounds on the parameters. $\mathbf{S}$ is a matrix containing the reciprocals of the data's standard deviations, such that $\mathbf{S}^T = \mathbf{D}^{-1}$. The current difference between calculated ($\mathbf{d}_i$) and observed data ($\mathbf{d}^{obs}$) is given by $\delta\mathbf{d}_i = \mathbf{d}^{obs} - \mathbf{d}_i$. The trade-off parameter λ is adjusted from large to small, as iterations proceed. That the fluid saturations sum to unity can be imposed as an additional constraining equation, $\mathbf{C}\mathbf{m}_i = \mathbf{h}$, where 1's in the rows of $\mathbf{C}$ multiply the saturations in $\mathbf{m}_{i+1}$, and the elements of $\mathbf{h}$ corresponding to sums of saturations equal 1. Elements of $\mathbf{h}$ that correspond to porosity are 0. The α is fixed at a value (100, in these examples) large enough to insure $\mathbf{C}\mathbf{m}_i = \mathbf{h}$ to within a very small tolerance. When variable layer thicknesses are added to the parameter vector, an additional row is added at the bottom of $\mathbf{C}$, with 1's at positions corresponding to layer thickness in the parameter vector, and an additional value equal to the desired total thickness of the variable layers is added to the end of $\mathbf{h}$. This addition provides the further constraint that the inversion interval has the total thickness of the reservoir interval.

The parameter covariance of $\mathbf{m}$ is

$$Cov(\mathbf{m}) = \mathbf{M}^{-1}\mathbf{J}^T\mathbf{S}^T\mathbf{S}\mathbf{J}\mathbf{M}^{-1}, \tag{4}$$

where

$$\mathbf{M} = (\mathbf{J}^T\mathbf{S}^T\mathbf{S}\mathbf{J} + \lambda\mathbf{W}^T\mathbf{W} + \alpha\mathbf{C}^T\mathbf{C}). \tag{5}$$

Standard errors of the parameters can be calculated from the diagonal terms of equation 4 and are displayed on the inversion model results that follow. Note that we are solving a regularized least-squares problem that forces the covariance (off-diagonal elements of equation 4) of model parameters to be high, a fact that is not captured in the display of parameter standard errors. In addition, because the solution is linearized at each iteration, if the minimum found is a local minimum rather than a global minimum, the parameter standard error estimated from equation 4 will be wrong. For these reasons, parameter standard errors should be considered qualitative only and should be used to compare relative parameter errors between inversions.

Many approaches exist for setting λ in the inversion. Constable et al. (1987) use a golden section search for determining λ, which requires on the order of ten additional forward-problem calculations per iteration, in addition to those required for calculation of the Jacobian. This approach is robust, but the run time requirements are impractical for full 3D CSEM inversion.

Instead, we have adopted a simpler approach described by Newman and Alumbaugh (1997) — an approach that has been demonstrated to be effective for large-scale CSEM problems. In this scheme, λ is selected as the iteration-weighted maximum row sum of the matrix product $[\mathbf{J}^T\mathbf{S}^T\mathbf{S}\mathbf{J}]$, where

$$\lambda = \underset{1 \le m \le np}{Max} \left| \sum_{j=1}^{np} a_{mj} \right| \Bigg/ 2^{(i-1)}. \tag{6}$$

Here, a_{mj} is an element of $[\mathbf{J}^T\mathbf{S}^T\mathbf{S}\mathbf{J}]$, np is the number of parameters, and i is the inversion iteration number.

ROCK-PROPERTIES MODEL

Direct inversion for the reservoir parameters requires a rock-properties model that links the reservoir parameters and geophysical parameters. The model we have adopted uses the Hertz-Mindlin (Mindlin, 1949) contact theory for the dry frame bulk (K_{dry}) and shear (G_{dry}) moduli of a dense, random pack of spherical grains. Modified Hashin-Shtrikman lower bounds (Hashin and Shtrikman, 1963) are used to calculate the effective moduli for porosities below the critical porosity. Dvorkin and Nur (1996) described using this procedure to model velocity-pressure relations for North Sea sandstones, and Hoversten et al. (2003) described its use in combined seismic and EM inversion. Archie's law (Archie, 1942) is used to model electrical resistivity as a function of ϕ and S_w. The fluid bulk moduli (K_{brine}, K_{oil}, K_g) and densities (ρ_{brine}, ρ_{oil}, ρ_g) of brine, oil, and gas, respectively, are computed using relations from Batzle and Wang (1992).

The field data examples we present in this paper come from the Troll field in the North Sea. Seismic rock-properties-model parameters are found by using a simplex algorithm to minimize L_1, given by equation 7.

$$L_1 = \sum_{1}^{N} |V_p^{obs} - V_p^{calc}| + \sum_{1}^{N} |\rho^{obs} - \rho^{calc}|, \tag{7}$$

where there are N values of V_p^{obs}, V_p^{calc}, ρ^{obs}, and ρ^{calc}: the sonic-log compressional velocity, model-calculated compressional velocity, log density, and model-calculated density, respectively. The units used in defining L_1 are meters per second and kilograms per cubic

meter, so that the velocity and density have approximately equal numerical magnitudes and hence equal weight in the value of L_1. If shear-velocity logs are available, the V_s data misfit can be added to L_1. To derive the rock-properties model, we used log data from a well approximately 4 km to the northeast of the site used for the inversion tests (to be discussed below).

Figure 4 shows the log data with the calculated fit over the reservoir interval. Table 1 shows the parameters fixed in the inversion (which are assumed to be known) and those determined by the regression. The values for the shear modulus, grain Poisson's ratio, and grain density are very close to that of feldspar. For the inversions of Troll field data, we used the parameters shown in Table 1.

The three parameters of Archie's law, C, m, and n, are found by linear regression in the $\log_{10}$ domain:

$$R_{bulk} = CS_w^{-m}\phi^{-n}. \tag{8}$$

Employing the S_w, R_{bulk}, and ϕ logs from the same well used for the seismic-model parameters yields values of 0.78 ohm-m, 1.31, and 0.14 for C, m, and n, respectively. The low value of n indicates very little sensitivity to porosity. This also was noted in developing Archie's law parameters for logs from the Snorre field in the North Sea (Hoversten et al., 2001) and was caused, in that case, by clay filling the pore space. We will discuss below the effects of the small value of n on our inversion for porosity.

SYNTHETIC EXAMPLE

To illustrate the properties of the individual inversions and the combined inversion of AVA and CSEM data, we have constructed a simple five-layer model, using the rock-properties parameters given in Table 1 and the Archie's law parameters given above. The synthetic AVA data are sampled at 2 ms for seven angles (7.2, 13.5, 19.7, 25.6, 31.1, 36.3, and 41.0°). Gaussian random noise was added, starting with a variance of 0.2 times the noise-free trace vari-
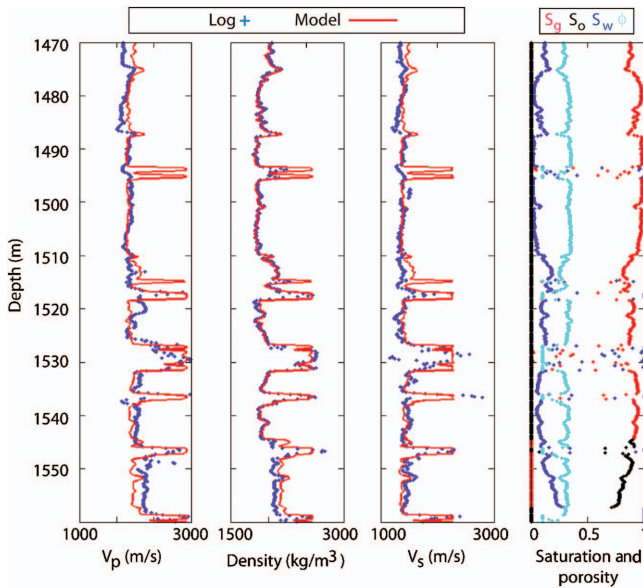
Table 1. Fixed parameters for regression of the rock-properties model and parameters determined from that regression.

Fixed parameters		Regression-fit parameters	
Critical porosity	0.38	Grain shear modulus	22.5
Oil API	28.5	Grain Poisson's ratio	0.34
Brine salinity	0.07	Grain density	2567
Gas gravity	0.59	No. of contacts/grain	13.5
Temperature (°C)	65		

ance for the first angle and increasing to 0.4 times the trace variance for the far angle. The CSEM data are the amplitude and phase of the electric field (electric field measured inline with the transmitting dipole source) at three frequencies (0.25, 0.75, and 1.25 Hz) for eight source-receiver offsets (0.775, 1.7, 2.5, 3.3, 4.1, 4.5, 5.7, and 6.5 km) from an electric dipole source 50 m off the seafloor and electric field receivers on the seafloor. Gaussian noise of 20% was added to the electric fields at the near offsets and increased to 40% at the maximum offset. The model has 1 km of seawater, with the target zone 1.4 km below the seafloor. Overburden (between seafloor and top of the target zone) conductivity is 1 ohm-m. The target zone comprises five 25-m-thick layers, each with variable ϕ and S_g, and with $S_o = 0$.

We tested two starting models: (1) all five layers with constant $S_g = 0.5$, $\phi = 0.2$ within the target zone; and (2) $S_g = (0.2, 0.7, 0.2, 0.7, 0.2)$, $\phi = (0.2, 0.2, 0.2, 0.2, 0.2,)$ for the five layers from top to bottom within the target zone. We present AVA-only, CSEM-only, and joint AVA-CSEM inversions to illustrate the sensitivities of the data used separately and together. The target rms misfit of the error-weighted data, 1.0, was reached in all inversions unless otherwise stated.

Both CSEM-only and AVA-only inversions that began with uniform $S_g = 0.5$ failed to converge to a model anywhere near the true model. Both inversions became trapped at a local minimum in the object function, far from the true model. For either CSEM-only or AVA-only inversions to converge to a nearly correct model, the starting model required the correct sign in the reflection coefficients at the top of the high S_g layers. This starting model, with layers 2 and 4 having higher S_g than the surrounding layers, produced individual inversions (CSEM-only and AVA-only) that distinguish the two high S_g layers.

Figure 5 shows the results of using the CSEM data only; Figure 6 shows the results of using only AVA data. Using only the CSEM data produced S_g estimates that are very close in the high S_g layers and no more than 0.08 off in the low S_g layers. However, the S_g standard deviations were large and only plot on the scale of the figure for the high S_g layers. The CSEM-only inversion provided essentially no information about the porosity.

The inversion of the AVA data produced better estimates of S_g in the top and bottom layers (low S_g), with much lower overall standard deviations of the parameters. The S_g estimate of the second high-S_g layer was less accurate than that of the CSEM inversion.

Figure 4. Log-obtained V_p, density, and V_s (blue crosses) compared with calculated values (red line from regression fit) are shown in the left three panels. Input saturations and porosity are shown in right panel.

Seismic inversion produced much better estimates of layer porosities when compared with the CSEM inversion.

For the joint inversion of both the CSEM and AVA data, each datum was weighted only by its assigned data errors. No relative weighting between CSEM and AVA data in equation 2 was used, although such weighting may be considered in certain circumstances if there is reason to believe that one data set should dominate (e.g., if the CSEM data are thought to be highly 3D, so that the 1D assumption is less valid for the CSEM than for the seismic data).

Figure 7 shows the S_g and ϕ estimates from jointly inverting both the CSEM and AVA data sets. The CSEM and AVA observed and calculated data from the joint inversion are shown in Figures 8 and 9, respectively. The starting model again was the constant S_g

and ϕ that had caused both the CSEM and AVA inversions to find local minima that were distant from the true model. Here, however, the CSEM data provided enough low-wavenumber information that when seismic data were added, the joint inversion did not get trapped in a local minima and produced a final model close to the true model.

In general, estimated S_g and ϕ were closer to the true values in the joint inversion than they were in either the AVA-only or CSEM-only inversions. The S_g estimates from the joint inversion were the same or better than those from the AVA-only inversion. In particular, the S_g estimates of the lower two layers were significantly closer to their true values in the joint-inverse model (Figure 7), compared with the estimates from the AVA-only inverse model (Figure 6).
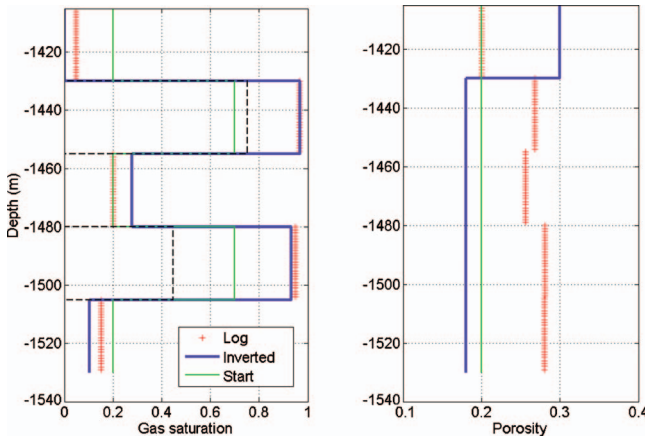

Figure 5. Electromagnetic-data-only inversion of the synthetic model's target zone. True values are plus symbols. Starting values (green line), from top to bottom layer, were $S_g = (0.2, 0.7, 0.2, 0.7, 0.2)$, $\phi = (0.2, 0.2, 0.2, 0.2, 0.2)$. Blue lines show final parameter estimates obtained from inversion. Black dashed lines represent ±1 standard deviation from the model parameters calculated using equation 4.

Figure 7. Inversion for (a) gas saturation and for (b) porosity of the synthetic model's target zone, using seismic AVA and CSEM data. True values are plus symbols. Starting values (green line) for all layers were $S_g = 0.5$ and $\phi = 0.2$. Blue lines show final parameter estimates obtained from inversion. Black dashed lines represent ±1 standard deviation from model parameters.
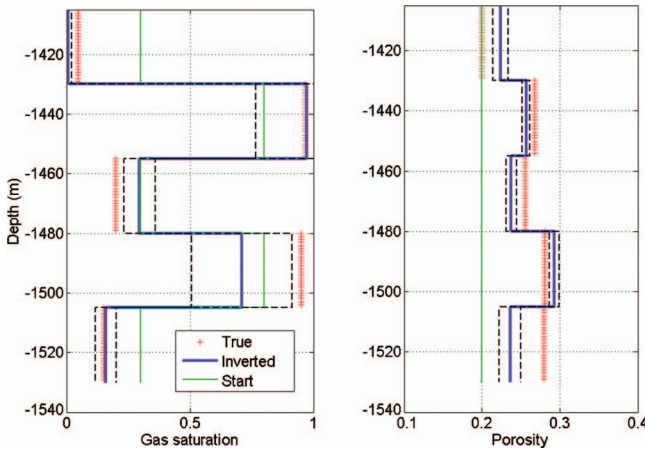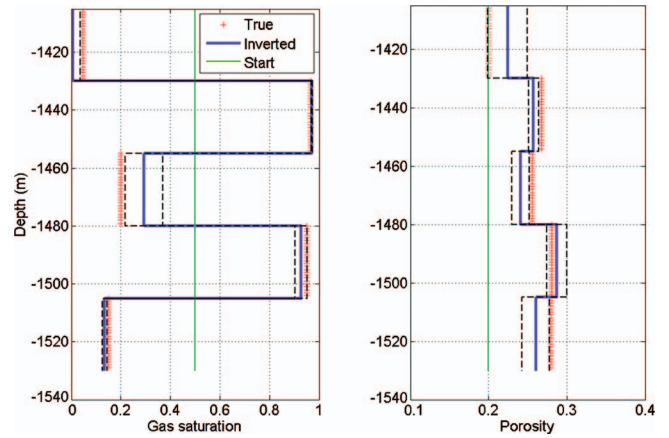

Figure 6. Seismic-data-only inversion of the synthetic model's target zone. True values are plus symbols. Starting values (green line), from top to bottom layer, were $S_g = (0.2, 0.7, 0.2, 0.7, 0.2)$, $\phi = (0.2, 0.2, 0.2, 0.2, 0.2)$. Blue lines show final parameter estimates from inversion. Black dashed lines represent ±1 standard deviation from model parameters.
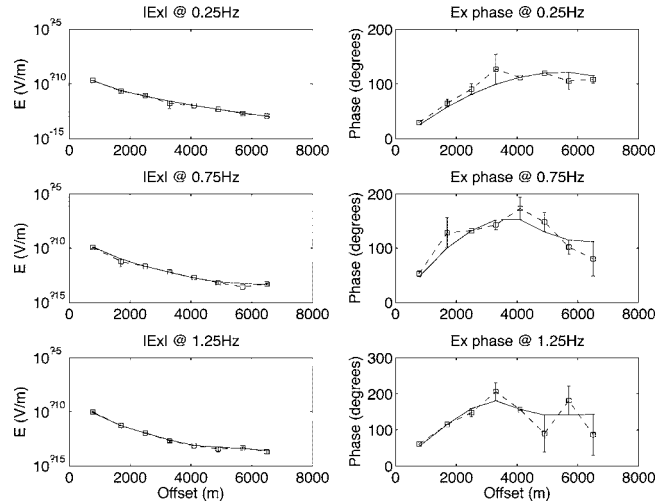

Figure 8. Synthetic marine CSEM data (dashed curves with error bars) from the true model and calculated data (solid curves) from the joint inversion of synthetic AVA and CSEM data to produce the inversion model shown in Figure 7. The left panels show amplitude of the received electric field and the right panels show the phase of the received electric field.

In addition, in the joint-inverse model the parameter standard deviations of the S_g estimates decreased. The standard deviations of the ϕ estimates were slightly increased in the joint-inverse estimates, compared with the seismic-only standard deviations. However, ϕ estimates for the first three layers were the same for the joint inversion and the AVA-only inversion, and the ϕ estimates of the lower two layers improved in the joint inversion.

Sensitivity to rock-properties-model parameters

For S_g and ϕ, inversion of either the CSEM data or the seismic data, either in isolation or in combination, relies on the parameters of the rock-properties model. Those parameters can be determined by laboratory core measurements and/or regression fits to log data, as described above and in Hoversten et al. (2003). To check the sensitivity of the inversion to errors in the rock-properties model, the joint inverse shown in Figure 7 was run successively with 5% errors in each of the rock-properties parameters, and the mean error for ϕ and S_g was calculated (Figure 10). The red line in Figure 10 shows the mean errors in the S_g and ϕ estimates with exact rock-properties parameters. The parameters that control dry frame bulk K_{dry} — grain density, grain shear modulus, critical porosity, number of grain contacts, and grain Poisson's ratio — are the most important. The inverse estimates of ϕ are less sensitive to rock-properties errors than is S_g.

The sensitivity to parameters controlling K_{dry} can be understood by considering the Hertz-Mindlin representation of K_{dry}:

$$K_{dry} = \left[\frac{l^2(1 - \phi_0)^2 G_{grain}^2}{18\pi^2(1 - v)^2} \cdot P_{eff} \right]^{1/3}, \qquad (9)$$

where ϕ_0 is the critical porosity (the porosity above which the grains become a liquid suspension), P_{eff} is the effective pressure, v

is the grain Poisson's ratio, G_{grain} is the grain shear modulus, and l is the average number of grain contacts per grain. Because K_{dry} is a nonlinear function of ϕ_0 l, v G_{grain}, and P_{eff}, we would prefer to use K_{dry} if core measurements of K_{dry} are available. When K_{dry} is used as a bulk parameter instead of calculating the bulk parameter from equation 9, 5% errors on K_{dry} produce approximately 7% and 4% errors for estimates of S_g and ϕ, respectively.

TROLL FIELD DATA

Seismic and marine CSEM data were acquired over a portion of the Troll field in 2003. Figure 11 shows the location of the marine CSEM line (dashed line between receiver sites 1 and 24). Well 31/2-1 intersects the reservoir beneath the CSEM transect, as shown by the arrow in Figure 11. The CSEM receiver units were laid out in a line, with a nominal separation of 750 m between locations 1 and 24. A 220-m electric dipole transmitter, producing an 800-amp square wave, was towed at approximately 2 knots along the receiver line in both directions. It produced data at the receivers for transmitters on either side of the receiver. The electric dipole transmitter was aligned nominally with the survey line, but course corrections and ocean currents produced some variation in the transmitter's orientation along the line. Received CSEM data, along with the transmitter locations and current, were recorded as a time series. In postprocessing, the CSEM time series were averaged to produce in-phase and out-of-phase electric fields for average transmitter locations spaced 100 m apart along the line. The transmitter fundamental was 0.25 Hz. Sufficient power existed to extract the third and fifth harmonics, so that three frequencies (0.25, 0.75, and 1.25 Hz) were acquired.
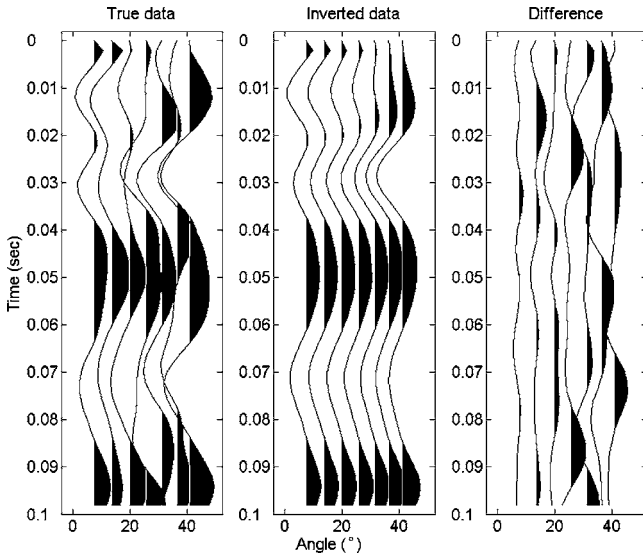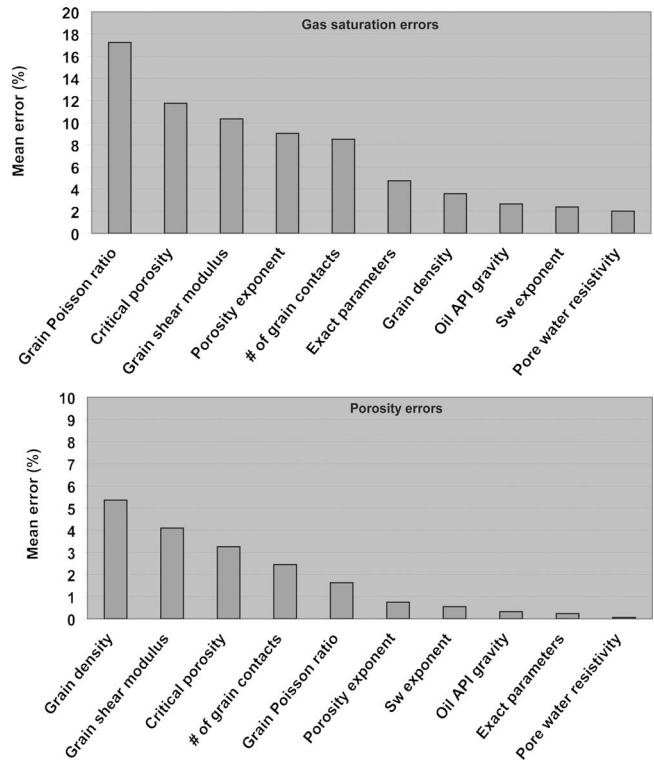

Figure 9. Observed data, calculated estimates, and difference AVA data for the joint-inversion model shown in Figure 7. (a) Synthetic data (considered to be observed data by inversion), with a variance that is equal to 0.2 times the noise-free trace variance at a low angle and that linearly increases to 0.4 times the noise-free trace variance at the far angle. (b) Calculated data from the joint-inversion model shown in Figure 7. (c) The difference between observed and calculated data.

Figure 10. Mean absolute errors in inversion parameters for 5% error in rock-properties parameters. (a) Mean errors in S_g estimates. (b) Mean errors in ϕ estimates.

Figure 12 shows the CSEM data converted to amplitude and phase of the electric field in the line direction (roughly parallel to the transmitter dipole orientation) from the receiver nearest the 31/2-1 well. If the earth had a 1D conductivity structure (as the inversion forward model assumes), the response, in terms of both amplitude and phase, would be identical for transmitters on either side of the receiver. We see that this was true for offsets less than or equal to about 4 km. For offsets beyond 4 km, the difference between data from transmitters on opposing sides of the receiver increased with offset and frequency. The largest asymmetry occurred, in both amplitude and phase, for the highest frequency at the farthest offsets.

In general, the spatial sensitivity of the CSEM data to this dipole-dipole configuration is a function of source-receiver offset, earth conductivity, and frequency, with lower frequencies and larger offsets showing sensitivity to deeper changes (Spies, 1989). As the transmitter-receiver offset increases, the centroid of the sensitivity region moves downward and away from the receiver, in the direction toward the transmitter. To approximate a 1D response, we averaged the EM data for transmitters on either side of the receiver, thus causing the centroid of the sensitivity region of the averaged data to be directly below the receiver location.

The 3D seismic data were prestack time migrated and sorted into common-midpoint gathers. Normal moveout (NMO) and residual NMO were applied, multiples were removed, and data were filtered to a nominal zero-phase wavelet. The offsets were converted to angles by ray-tracing a layered model with velocity and density taken from the 31/2-1 well. Depth-time pairs were generated from the 31/2-5 well and used to determine the time window for the seismic data, such that the data covered the depth interval 100 m above and below the reservoir zone.

Data for comparison and conditions of inverse models

No production had occurred in the area of the 31/2-1 well, where our data analysis takes place. The nearest production is from the oil rim (approximately 13-m thick), several kilometers from our site. We expected that S_w has not changed by more than 1% or 2% since the logs were taken. The high gas-saturation zone extends from 1415 to 1544.5 m. A zone predominantly of oil exists between 1544.5, the gas-oil contact (GOC), and 1557.5 m, where original oil saturations were between 70% and 85%. Between 1557.5-m depth and the bottom of the logged interval, at 1670 m, there is a paleo-oil-zone where original oil saturations were 20 to 30%. No gas- or oil-saturation logs are available, but time-lapse seismic data have been interpreted as follows: Between the time of log measurements and the geophysical surveys used in this paper, production from the oil rim lowered reservoir pressures enough that gas was released from the oil in the oil- and paleo-oil-zones, resulting in a 5% increase in gas saturation in these zones. Thus, we used the logged S_w to calculate oil and gas saturation as follows: Above 1544.5 m, oil saturation (S_o) is assumed to be zero, and we assume $S_g = 1 - S_w$; below 1544.5 m, $S_o = 1 - S_w - 0.05$ and $S_g = 0.05$.

We used the logged S_w and calculated S_g and S_o for comparing the performance of the different inversions. In addition to visual inspection of the results, we calculated three measures of agreement between the inversion predictions and the logs:

$$rms = \sqrt{\frac{\int_{z_1}^{z_2} [l(z) - i(z)]^2 dz}{z_2 - z_1}}, \qquad (10)$$

$$L_1 = \int_{z_1}^{z_2} |l(z) - i(z)| dz, \qquad (11)$$
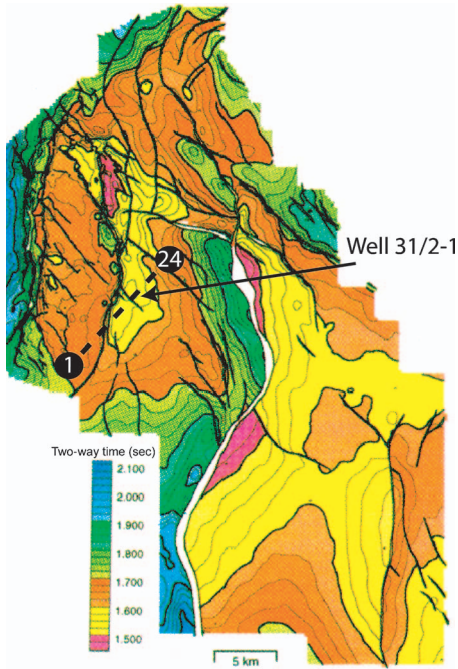

Figure 11. Troll top reservoir (Sognefjord) two-way traveltime in seconds (after Hwang and McCorkindale, 1994). The dashed line is the marine CSEM line from receivers 1 to 24. The black arrow points to the intersection of well 31/2 − 1 with the vertical plane containing the CSEM line.
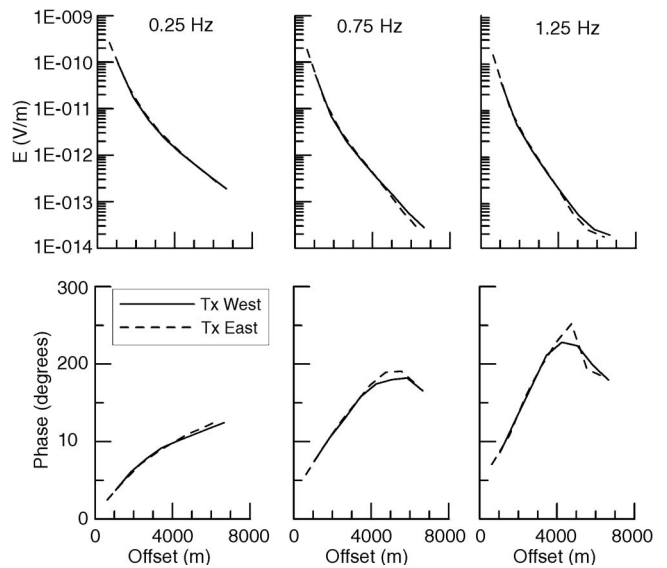

Figure 12. Electric-field amplitude normalized by the transmitter moment (upper row) and phase (lower row) at 0.25, 0.75, and 1.25 Hz as a function of the source-receiver offset (m) at a CSEM receiver near the 31/2 − 1 well. Transmitter locations to the west of the receiver are plotted as a solid line, and transmitter locations to the receiver's east are plotted as a dashed line.

$$\Delta = \left| \int_{z_1}^{z_2} [l(z) - i(z)]dz \right|, \qquad (12)$$

where $l(z)$ is the logged value at depth z and $i(z)$ is the inverted value. The rms measure is in units of saturation or porosity, and the latter measures have units of thickness (m).

The starting model for all inversions of the Troll field data had linear ramps in S_w and S_g such that S_w went from 0 to 1 and S_g went from 1 to 0, moving downward from the top to the base of the reservoir. The initial S_o was set to zero. Starting values for ϕ came from blocking the ϕ log. The bounds used in the quadratic programming solver of equation 3 were set at ±0.3 for S_w and S_g (subject to a minimum and maximum of 0 and 1, respectively) and at ±0.1 for ϕ, from their initial values. The upper bound on S_o was 0.1 above 1544.5 m, where no oil was present in the original logs. Below 1544.5, the S_o upper bound began at 0.7 at 1544.5 and decreased linearly to 0.1 at the base of the reservoir, to allow oil where it originally was present. The lower bound on S_o was zero everywhere.

A sparse-spike acoustic impedance (AI) inversion (Levy and Fullagar, 1981) was first done on the zero-offset AVA trace. The layering from the acoustic-impedance inversion was used to determine the minimum number of layers required in the reservoir interval. Initial inversions were begun with the layer thicknesses determined from the AI inversions in time and converted to depth using the log acoustic velocities. However, we found that inversions starting with uniform layer thickness performed better than those starting with thicknesses derived from the AI time layers and assuming the log velocities. Thus, the results shown in subsequent figures began with the number of layers determined from the AI inversion with a uniform thickness of 20 m.

Because the inversions began with a large value of λ used in equation 1 (on the order of 1000, as determined by equation 6), the smoothing term dominated the initial iterations and produced the flattest model within the bounds on the first iteration. The starting models shown in Figure 13 are the input starting models before the first iteration. In subsequent inverse-model plots for the AVA-only and joint AVA-CSEM inversions, we show the model after the first
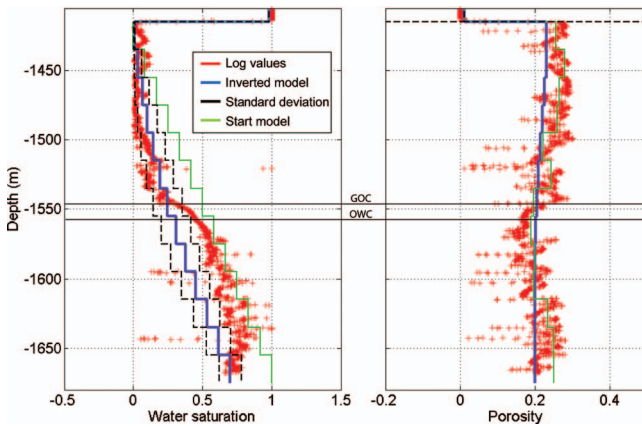
iteration had smoothed the input model, because that is effectively where the algorithm begins. The rms misfit of the target data was 1.0. For all examples, the minimum rms was found within 40 iterations. The target interval was divided into thirteen 20-m-thick layers, with five seismic layers above and one seismic layer below the target zone. The conductivity overburden consisted of 13 layers above the target zone. In addition to fluid saturations and ϕ in the target zone, layer thicknesses were added as inversion parameters in the AVA-only and joint AVA-CSEM inversions, to accommodate placement of the sparse reflection coefficients.

CSEM-only inversion

Results of inversion of the CSEM data nearest the 31/2-1 well (Figure 12) are plotted in Figure 13. The rms data misfit achieved was 1.05. The CSEM data could not distinguish between oil and gas because the electrical resistivity is a function of S_w and ϕ only. Thus, only these parameters were used in the CSEM-only inversion. The observed and calculated CSEM data are shown in Figure 14. At the top of the reservoir, S_w was 0.04, and that value increased with depth. The inversion reduced S_w from its value in the starting model at the bottom of the reservoir and smoothed out the blocked log-porosity starting values to a mean porosity of 0.21; porosity was higher in the top 100 m of the reservoir. The inversion reflects the relative sensitivity of the bulk resistivity to S_w and ϕ, as discussed in the rock-properties section above. Standard deviations for S_w were small at the top of the reservoir (because the CSEM response is most sensitive to the presence of a resistor at the top of the reservoir) and increased with depth, whereas standard deviations for ϕ were too large to plot on the scale of the figures (average standard deviation for ϕ over the reservoir interval was 2.2). A very small Archie's-law porosity exponent (low sensitivity to ϕ) translated to high variance in ϕ estimates.

AVA-only inversion

Inversions of AVA-only data and combined AVA-CSEM data were parameterized by S_w, S_g, S_o, ϕ, and layer thickness within the reservoir zone. Figure 15 shows the inverse model from inversion of the AVA-only data nearest the 31/2-1 well. The observed and calculated AVA data are shown in Figure 16. The rms data misfit

Figure 13. Inversion for (a) S_w and (b) ϕ using only CSEM data. Red plus signs are log values, the green line is the starting model, and the blue line is the final inversion model. Black dashed lines are the one-standard-deviation bounds. Porosity bounds are too large to plot on the figure, with the average standard deviation equal to 2.2.
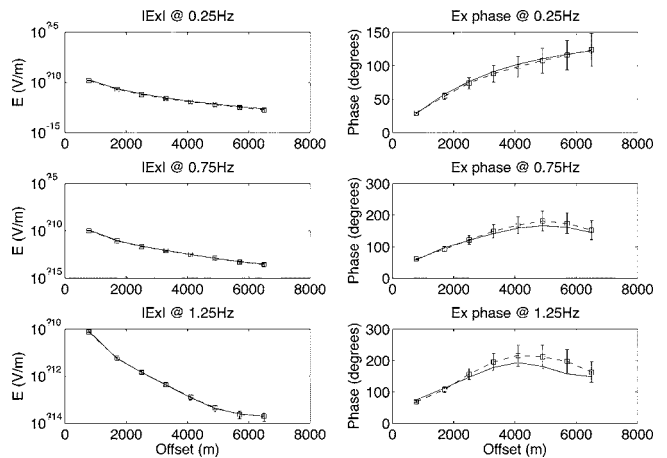

Figure 14. Observed and calculated (a) inline electric field (E) amplitude and (b) phase for the CSEM-only inversion model shown in Figure 13. The total rms data misfit is 1.05.

achieved was 0.87. The inversion decreased S_w and increased S_g from their starting values in the upper 100 m of the reservoir. Porosity (ϕ) estimates were much closer to logged values than in the case of the CSEM-only inversion, with significantly smaller ϕ standard deviations compared with those in the CSEM-only inversion. All inversions that included AVA data produced ϕ estimates with low standard deviations. This is consistent with the high sensitivity of the AVA response to changes in porosity, as shown in Figure 1. The inversion estimated the presence of gas and water (brine) in the lower half of the reservoir, rather than the oil that is

present. The depths of the top of gas, the gas-oil contact, the top of the paleo-oil-zone, and the base of the logged interval are marked T1, T2, T3, and T4, respectively, at points in time that were converted using the log velocity.

Joint AVA-CSEM inversion

Figure 17 shows results of the simultaneous inversion of the CSEM and AVA data. The calculated AVA data are visually indistinguishable from those shown in Figure 16. The combined rms data misfit was 0.91, which is slightly higher than that for the AVA inversion shown in Figure 16. The joint inversion decreased S_w and increased S_g in the top 100 m of the reservoir, much as the AVA-only inversion did. However, the saturation estimates were much closer to the logged values from the lower half of the reservoir than were saturation estimates from the AVA-only inversion. Here, the S_g has been reduced to nearly zero from the starting model, and S_o
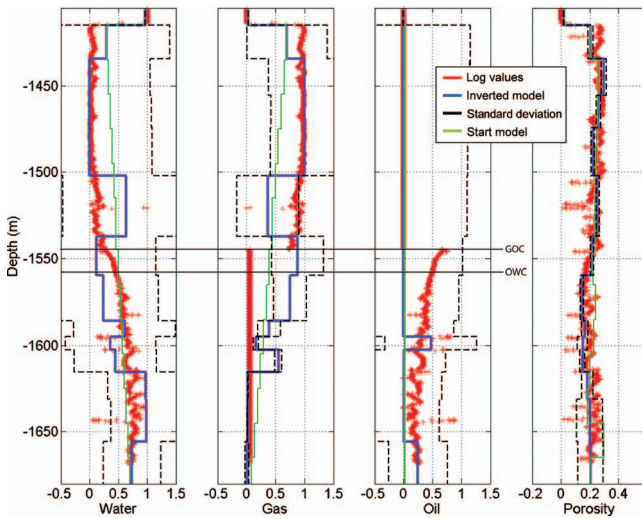

Figure 15. Inversion estimates of water, gas, oil, and porosity using only seismic AVA data. Red plus signs are log values, the green line is the parameter values after the first iteration (when smoothing has flattened the starting model), and the blue line is the final inversion model. Black dashed lines are one-standard-deviation bounds for the model parameters.

Figure 17. Inversion for (a) water, (b) gas, (c) oil, and (d) porosity, using both seismic AVA and CSEM data. Red plus signs are log values, the green line is the parameter values after the first iteration, and when smoothing has flattened the starting model, blue line is final inversion parameters. Black dashed lines are one-standard-deviation bounds.
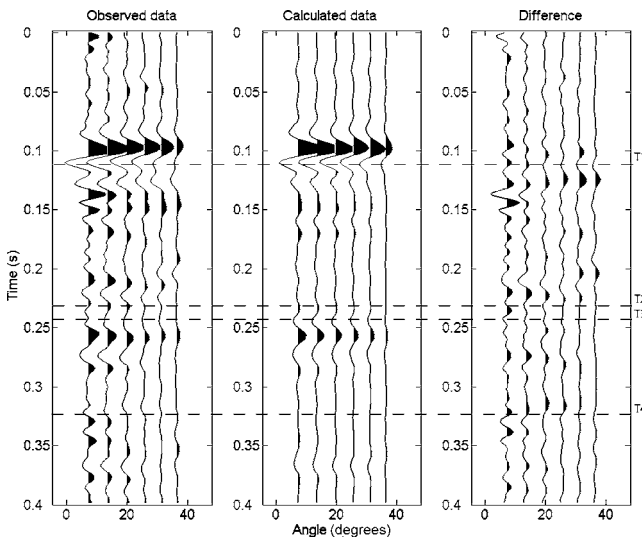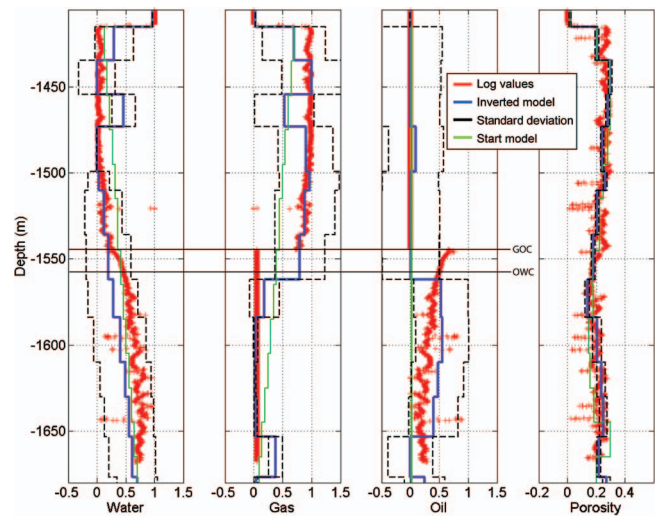

Figure 16. Observed (a) seismic AVA gather data, (b) calculated AVA data from the AVA-only inversion shown in Figure 15, and (c) the difference between observed and calculated AVA data. Zero time corresponds to a depth of 1300 m. Times marked as T1, T2, T3, and T4 on the right side of the figure correspond to top of gas, gas-oil contact, top of paleo-oil zone, and bottom of the logged interval, respectively. The rms data misfit is 0.87.
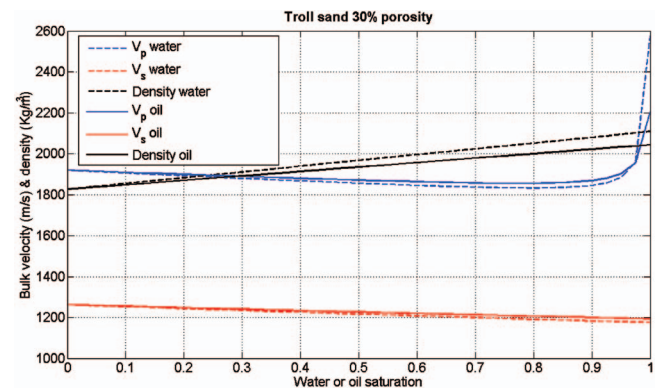

Figure 18. Reservoir bulk acoustic (blue) values, shear velocity (red) values, and density (black) values calculated as a function of water or oil saturation, using the rock-properties model derived from logs and used in the inversions shown in Figures 15 and 17.

has been added. The addition of CSEM data has caused a reduction in the S_w in the lower half of the reservoir (as the CSEM-only inversion did), so that the S_w estimates from the joint inversion fall between those of the CSEM-only and the AVA-only estimates. The standard deviations have been reduced for all parameters, but most significantly for S_w and S_o, compared with the AVA-only inversion results shown in Figure 15.

We note that the S_w levels in this interval (1550 m to 1670 m) correspond to S_w levels at which V_p is least sensitive to changes in S_w.

Figure 18 shows the computed V_p, V_s, and ρ (density) from the rock-properties model used in the inversion for brine-gas and oil-gas combinations. Velocity of P-waves, V_p, had a minimum at $S_w = 0.8$, and varied only slightly, between $S_w = 0.9$ and 0.6. The S_w in the lower half of the reservoir interval was mostly in this range. In addition, the V_p and V_s sensitivities to substitution of oil or brine were very small. The differences in V_p, V_s, and density values between a brine:gas mix of 80%:20% and an oil:gas mix of the same ratio were only 1.2%, 1.0%, and 2.4%, respectively. The insensitivity of the seismic parameters to any exchange of oil or brine caused the AVA-only inversion to substitute brine for oil in the lower half of the reservoir. The advantage introduced by adding the CSEM data in the joint inversion is that it constrains S_w. With that added constraint, the AVA data could distinguish between oil and gas saturations in the lower portion of the reservoir. Both AVA-only and joint AVA-CSEM inversions produced very similar ϕ estimates, the sensitivity to ϕ coming mostly from the AVA data. However, in general, the combined inversion provided smaller standard deviations for the parameters than did either CSEM-only or AVA-only inversions.

None of the inversions (CSEM-only, AVA-only, or CSEM-AVA) resolved the correct location of the GOC at 1544.5 m. The CSEM data alone did not have the spatial resolution to locate the GOC. The event on the AVA gathers that is marked T2 in Figure 16 corresponds to the depth of the GOC, and both the AVA-only and the joint CSEM-AVA inversions have matched this portion of the AVA data. Examination of the velocity and resistivity logs shows that the velocity and resistivity transitions are smooth through the oil zone, from the GOC into the paleo-oil-zone. In this portion of the reservoir, surrounding hard streaks and porosity changes produce variations in velocity (and in reflection coefficients) that are greater than the velocity variations caused by the GOC. On the basis of the resistivity and velocity logs, we believe that the transition in S_g at the GOC is not as sharp as that indicated in the calculated S_g and S_o logs shown in Figures 15 and 17. We also believe that the inversion results reflect this fact.

The CSEM data misfit for the joint inversion is visually identical to that shown in Figure 15 for the CSEM-data-only inversion. The slight increase in the data misfit for the AVA-CSEM inverse compared with the AVA-only misfit (0.91 compared with 0.87) results entirely from an increase in the CSEM data misfit in the joint inversion. As the AVA-CSEM inversion iterations progressed, the CSEM data were fitted first by the relatively smooth (high λ) models. As the iterations increased and λ decreased, admitting rougher models, the AVA data misfit decreased and the CSEM data misfit increased. Inconsistencies between the AVA and CSEM rock-properties models and differences in the spatial sensitivity of the two data sets are two likely sources of decreased data fit in the joint inversion.

Table 2 shows the numerical measures, defined above, for the agreement between the inversion estimates of fluid saturations and ϕ and the actual data for those parameters, measured from the logs. The lowest values (lowest rms or best agreement with the log values) are highlighted in bold type. The joint inversion produced the lowest rms and L_1 norm fit to the S_g, S_o, and ϕ logs, as well as the net S_g, S_o, and ϕ closest to the log over the reservoir interval. The CSEM inversion produced the lowest rms and L_1 norm fit to S_w. The AVA-only inversion produced the lowest net S_w over the reservoir interval — slightly better than that produced by the CSEM-only inversion.

DISCUSSION AND CONCLUSIONS

We have developed an algorithm for joint AVA and CSEM inversion. Tests of this algorithm on synthetic 1D models representing gas and petroleum reservoir scenarios show that combining AVA and CSEM data in an inversion to estimate reservoir parameters produces better estimates, with lower variance, than does either a CSEM inversion or an AVA inversion performed separately. Analysis of error propagation through the rock-properties model shows that errors in the parameters of the rock-properties model introduce errors of comparable size (in terms of percent) in the joint-inversion estimates of reservoir parameters. Errors introduced by the rock-properties model can be reduced if laboratory-derived values for the dry-frame bulk modulus can be used (as opposed to computing the dry-frame bulk modulus from the nonlinear relations of the Hertz-Mindlin model). Field-data inversion results from the North Sea Troll field are consistent with synthetic model results. Gas and oil saturation and porosity estimates from joint inversion are closer to the logged values, by all numerical measures, than are estimates from either CSEM or AVA inversion done separately. For water saturation, the CSEM-only inversion estimate is the closest to the logged values.

The benefits of combining CSEM data with AVA data are more striking in synthetic tests than in the field-data example presented here, although the joint inversion of field data does produce closer agreement with logged values of S_g, S_o, and porosity, with lower

Table 2. Numerical measures of fit between the inversion estimates of fluid saturations (S_w, S_g, and S_o) and ϕ compared with the 31/2 − 1 well logs. Log values integrated over the inversion interval (1405–1697 m) are: S_w = 96.32, S_g = 126.64, S_o = 39.92, and ϕ = 56.23 (units of saturation or porosity — meters). The differences between the estimated and logged net values over the inversion interval are annotated as Δ. The best numbers (values with the lowest rms, or values closest to the net log values) are highlighted in bold type.

	S_w rms	S_w L_1	ΔS_w	S_g rms	S_g L_1	ΔS_g	S_o rms	S_o L_1	ΔS_o	rms	L_1	$\Delta\phi$
CSEM	**0.15**	**192**	15.84	na	na	na	na	na	na	0.045	60	2.74
AVA	0.27	356	**13.1**	0.38	459	19.96	0.23	459	33.22	0.049	67	1.98
Joint CSEM-AVA	0.21	292	14.78	**0.25**	**271**	**6.4**	**0.2**	**271**	**7.62**	**0.044**	**57**	**0.76**

parameter standard deviations, than does inversion of either type of data done in isolation. Part of the difference between performance of the joint inversion on synthetic data and on field data is certainly a result of the large number of unknown noise sources inherent in the field data. These include noise in the estimated angle-dependent wavelets and the possible presence of correlated (non-Gaussian) noise in both CSEM and AVA data sets. The saturation and porosity logs themselves, used for comparison to the inversions, can be in error. In addition, the 1D model may not accurately represent the actual earth. This is more likely to be a problem for the CSEM data (which have a larger spatial footprint) than it is for the AVA modeling, although the assumption that all multiples have been removed and that true relative amplitudes have been recovered in the seismic data also may not be strictly valid.

Many of the assumptions inherent in the algorithms presented here can be overcome by increasing the complexity of both the seismic model and the CSEM model. The next improvement to be investigated would be the use of a 1D elastic seismic calculation that would include all multiples, mode conversions, and waveform spreading. The CSEM calculation will move from 1D to 3D. Both of these advances require significantly more computer time, with the 3D CSEM calculations dominating the computing budget and requiring implementation for parallel cluster computing. Such work currently is under way.

It is also worthwhile to consider different types of seismic data for combination with CSEM data. In particular, seismic traveltime tomography may provide a better (and certainly different) companion for CSEM data, in that it would yield a more comparable spatial scale of resolution.

The limitations described above notwithstanding, benefits arise from combining CSEM data with seismic data through joint inversion. We hope that this work will stimulate others to continue the investigation.

ACKNOWLEDGMENTS

REFERENCES

Aki, K., and P. G. Richards, 1980, Quantitative seismology: Theory and methods: W. H. Freeman and Co.
Archie, G. E., 1942, The electrical resistivity log as an aid in determining some reservoir characteristics: Transactions of the AIME, **146**, 54–62.
Batzle, M., and Z. Wang, 1992, Seismic properties of pore fluids: Geophysics, **57**, 1396–1408.
Buland, A., M. Landro, M., Andersen, and T. Dahl, 1996, AVO inversion of Troll field data: Geophysics, **61**, 1589–1602.
Buland, A., and H. More, 2003, Bayesian linearized AVO inversion: Geophysics, **68**, 185–198.
Castagna, J. P., AVO analysis — Tutorial and review, 1993, *in* J. P. Castagna, and M. M. Backus, eds., Offset-dependent reflectivity — Theory and practice of AVO analysis: SEG Investigations in Geophysics, no. 8, 3–36.
Constable, S. C., 1990, Marine electromagnetic induction studies: Surveys in Geophysics, **11**, 303–327.
Constable, S., and C.S. Cox, 1996, Marine controlled source electromagnetic sounding 2. The PEGASUS experiment: Journal of Geophysics Research, **101**, 5519–5530.
Constable, S., A. Orange, G.M. Hoversten, and H.F. Morrison, 1998, Marine magnetotellurics for petroleum exploration part 1: A seafloor equipment system: Geophysics, **63**, 816–825.
Constable, S. C., R. L. Parker, and C. G. Constable, 1987, Occam's inversion — A practical algorithm for generating smooth models from electromagnetic sounding data: Geophysics, **52**, 289–300.
Debski, W., and A. Tarantola, 1995, Information on elastic parameters obtained from the amplitudes of reflected waves: Geophysics, **60**, 1426–1436.
Drufuca, G., and A. Mazzotti, 1995, Ambiguities in AVO inversion of reflections from a gas sand: Geophysics, **60**, 134–141.
Dvorkin, J., and A. Nur, 1996, Elasticity of high-porosity sandstones: Theory for two North Sea data sets: Geophysics, **61**, 1363–1370.
Ellingsrud, S., T. Eidesmo, S. Johansen, M. C. Sinha, L. M. MacGregor, and S. Constable, 2002, Remote sensing of hydrocarbon layers by seabed logging (SBL): Results from a cruise offshore Angola: The Leading Edge, **21**, 972–982.
Evans, R. L., P. Tarits, A. D. Chavez, A. White, G. Heinson, J. H. Filloux, H. Toh, N. Seama, H. Utada, J. R. Booker, and M. J. Unsworth, 1999, Asymmetric electrical structure in the mantle beneath the East Pacific Rise at 17 degrees S: Science, **286**, 752–756.
Fletcher, R., and M. P. Jackson, 1974, Minimization of a quadratic function of many variables subject only to lower and upper bounds: IMA Journal of Applied Mathematics, **14**, 159–174.
Gallardo, L. A., and M. A. Meju, 2003, Characterization of heterogeneous near-surface materials by joint 2D inversion of DC resistivity and seismic data: Geophysical Research Letters, **30**, 1658 .
Hashin, Z., and S. Shtrikman, 1963, A variational approach to the elastic behavior of multiphase materials: Journal of the Mechanics and Physics of Solids, **11**, 127–140.
Hoversten, G. M., S. C. Constable, and H. F. Morrison, 2000, Marine magnetotellurics for base salt mapping: Gulf of Mexico field test at the Gemini Structure: Geophysics, **65**, 1476–1488.
Hoversten, G. M., R. Gritto, J. Washbourne, and T. M. Daley, 2003, Pressure and fluid saturation prediction in a multicomponent reservoir, using combined seismic and electromagnetic imaging: Geophysics, **68**, 1580–1591.
Hoversten, G. M., H. F. Morrison, and S. Constable, 1998, Marine magnetotellurics for petroleum exploration, Part 2: Numerical analysis of subsalt resolution: Geophysics, **63**, 826–840.
Hoversten, G. M., G. A. Newman, H. F. Morrison, E. Gasperikova, and J. I. Berg, 2001, Reservoir characterization using crosswell EM inversion: A feasibility study for the Snorre field, North Sea: Geophysics, **66**, 1177–1189.
Hoversten, G. M., and M. Unsworth, 1994, Subsalt imaging via seaborne electromagnetics: Proceedings of the 26th Annual Offshore Technology Conference, Houston, Texas, 26, 231–240.
Hwang, L.-F., and D. McCorkindale, 1994, Troll field depth conversion using geostatistically derived average velocities: The Leading Edge, **13**, 262–269.
Landro, M., 2001, Discrimination between pressure and fluid saturation changes from time-lapse seismic data: Geophysics, **66**, 836–844.
Levy, S., and P. K. Fullagar, 1981, Reconstruction of a sparse spike train from a portion of its spectrum and application to high-resolution deconvolution: Geophysics, **46**, 1235–1243.
Lumley, D., M. Meadows, S. Cole, and D. Adams, 2003, Estimation of reservoir pressure and saturations by crossplot inversion of 4D seismic attributes: 73rd Annual International Meeting, SEG, Expanded abstracts: 1513–1516.
MacGregor, L., M. Sinha, and S. Constable, 2001, Electrical resistivity structure of the Valu Fa Ridge, Lau Basin, from marine controlled-source electromagnetic sounding: Geophysical Journal International, **146**, 217–236.
Mindlin, R. D., 1949, Compliance of elastic bodies in contact: Transactions of ASME (American Society of Mechanical Engineers), **71**, A-259.
Newman, G. A., and D.L. Alumbaugh, 1997, Three-dimensional massively parallel electromagnetic inversion — I. Theory: Geophysical Journal International, **128**, 345–354.
Newman, G. A., and G.M. Hoversten, 2000, Solution strategies for two- and three-dimensional electromagnetic inverse problems: Inverse Problems, **16**, 1357–1375.
Plessix, R.-E., and J. Bork, 2000, Quantitative estimate of VTI parameters from the AVA responses: Geophysical Prospecting, **48**, 87–108.
Sen, M. K., and P. L. Stoffa, 1995, Global optimization methods in geophysical inversion: Elsevier.
Spies, B. R., 1989, Depth of investigation in electromagnetic sounding

methods: Geophysics, **54**, 872–888.

Tarantola, A., 1987, Inverse problem theory: Methods for data fitting and model parameter estimation: Elsevier.

Tikhonov, A. N., and V. Y. Arsenin, 1977, Solutions to ill-posed problems: John Wiley and Sons.

Tseng, H., and K. Lee, 2001, Joint inversion for mapping subsurface hydrological parameters: 71st Annual International Meeting, SEG, Expanded Abstracts, 1341–1344.

Tura, A. C., and D. Lumley, 1999, Estimating pressure and saturation changes from time-lapse AVO data: 69th Annual International Meeting, SEG, Expanded Abstracts, 1655–1658.

Ward, S. H., and G. W. Hohmann, 1987, Electromagnetic theory for geophysical applications, *in* M. N. Nabighian, ed., Electromagnetic methods in applied geophysics 1, Theory: SEG Investigations in Geophysics, no. 3, 131–228.

Webb, S. C., and D. W. Forsyth, 1998, Structure of the upper mantle under the EPR from waveform inversion of regional events: Science **280**, 1227–1229.